Numerical evaluation of a two-body point absorber wave energy converter with a tuned inerter

Keita Sugiura[a], Takehiko Asai[b]

[a]Graduate School of Systems and Information Engineering, University of Tsukuba, Japan
[b]Faculty of Engineering, Information and Systems, University of Tsukuba, Japan

Abstract

Ocean wave energy has been considered as one of the prospective renewable energy sources. To increase the amount of energy captured from ocean waves more, this article proposes a two-body point absorber wave energy converter (WEC) with a tuned inerter. The tuned inerter mechanism employed here consists of a spring, a linear damping element, and an inerter. This mechanism was originally proposed in the field of civil engineering as a structural control device which can absorb energy from vibrating structures effectively by taking advantage of the resonance effect of the inerter. In addition to the tuned inerter mechanism using a generator as the linear damping element, the current of the generator for the power take-off system is controlled based on the algorithms proposed in literature to achieve further improvement of the power generation performance. In this research, a detailed analytical model of the proposed two-body point absorber WEC is introduced and the equation of motion and the state-space representation are developed. Then the power generation performance for the JONSWAP spectrum is assessed and the effectiveness of the tuned inerter mechanism for two-body point absorber WECs is shown through numerical simulation studies.

Keywords: wave energy converter, two-body point absorber, tuned inerter, renewable energy, energy harvesting

1. Introduction

Ocean has been expected to be a promising renewable energy source since more than 70% of the Earth's surface is covered with oceans. However, compared with other renewable energy sources such as wind and solar energy, ocean energy conversion technology has not yet shown a strong presence in the renewable energy market. Since the concept of wave energy converter (WEC) was introduced by a former Japanese naval commander, Yoshio Masuda (1925-2009) [1], considerable effort has been devoted to develop a variety of WECs [2, 3, 4, 5] to exploit wave power in the ocean effectively. And various types of WECs proposed so far includes oscillating water columns [6, 7], oscillating bodies [8, 9, 10], and overtopping devices [11, 12, 13]. Among these devices, point absorbers consisting floating bodies are categorized as the oscillating body WEC and more expectations have been placed on this type of WEC because of its availability in deep offshore regions and its extensibility by arraying many buoys.

To improve the power generation performance of a conventional single-body point absorber WEC, which has one floating buoy, the authors employed a tuned inerter mechanism [14, 15]. Originally, the tuned inerter mechanism was proposed by [16] as a structural control device to absorb vibration energy effectively from vibrating civil structures such as buildings induced by seismic disturbances and to mitigate damage. This mechanism consists of a tuning spring, a linear damping element, and an inerter [17]. The inerter is an element to produce a force proportional to the difference between the accelerations of both ends and realized by devices such as a ball screw and a rack and pinion. In the tuned inerter mechanism, the damping element is installed in parallel with the inerter and these two elements are connected to the spring in series. Thus, once the spring stiffness is tuned so that the inerter resonates with the dominant frequency of the input vibration to the device, the deformation of the damping part is increased and the vibration energy is dissipated more effectively.

The authors employed a generator or a motor as the linear damping element in the tuned inerter mechanism and showed that the mechanism enhances the ability to extract energy from vibrating structures at a low frequency of less than 10 Hz [18, 19]. In addition, the authors proposed a single-body point absorber WEC with a tuned inerter and the efficacy of the present device was shown through numerical simulation studies [14] and wave flume testing using a small-scale prototype model [15].

While, generally, in the research community of point absorber WECs, a two-body point absorber WEC [20, 21, 22, 23] consisting a floating buoy and a submerged body is considered a preferable device from the view point of cost and deployment. This is because it does not need to connect to the ocean floor directly. Additionally, the two-body type has the potential to improve the power generation capability more than the single-body type by designing the two bodies to achieve a greater relative velocity between the two bodies.

The primary objective of this paper is to propose a two-body point absorber WEC with a tuned inerter. A detailed analytical model including the coupled force between the two bodies for the proposed WEC and the drag force is introduced and the equation of motion and the state-space representation are developed. Then the energy harvesting performance for the JONSWAP spectrum is assessed by comparing with a typical two-body point absorber WEC without the proposed mechanism. Secondly, the effectiveness of the current control of the generator for the power take-off (PTO) system of the proposed WEC is investigated. As control algorithms, two controllers proposed in [24], i.e., static admittance (SA) control and performance guaranteed (PG) control, are applied to capture more energy. The obtained results of the numerical studies using WATMIT [25] are shown and conclusions gained from this research follow.

It should be noted that we make use of the short-hand $\mathbf{G} \sim \left[\begin{array}{c|c} \mathbf{A} & \mathbf{B} \\ \hline \mathbf{C} & \mathbf{D} \end{array}\right]$ to imply $\mathbf{G}(s) = \mathbf{C}[s\mathbf{I} - \mathbf{A}]^{-1}\mathbf{B} + \mathbf{D}$ and $\hat{f}(\omega)$ denotes the Fourier transform of a function $f(t)$ in this article. Also, note that j is the imaginary unit such that $j^2 = -1$ and that the expected value is denoted by $\mathcal{E}\{\cdot\}$.

2. Modeling

To implement numerical studies, the analytical model of the proposed WEC is developed here as well as the models of the hydrodynamic forces, drag forces, and the JONSWAP spectrum. For simplicity, we consider the heave direction only because this motion becomes dominant for the power extraction of wave energy. Additionally, the generated power is defined in this section. Note that the floating buoy and the submerged body are indicated by 1st and 2nd bodies, respectively, in this article.

2.1. Conventional two-body point absorber WEC

For comparison, a conventional two-body point absorber WEC consisting a floating buoy (1st body) and a submerged body (2nd body) shown schematically in Fig. 1 (a) is reviewed briefly first. A PTO system including a generator is placed between these two bodies. In this research, it is assumed that the floating buoy has a circular cylinder shape with a diameter D_1 and

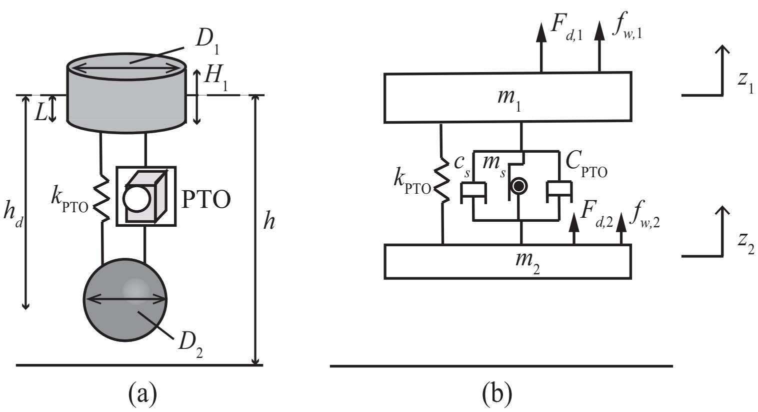

Figure 1: Conventional two-body point absorber WEC: (a) Schematic illustration, (b) Model.

the submerged body is a sphere with a diameter D_2. Also, the distance between these bodies is h_d at the static equilibrium position and these bodies are connected by a spring whose stiffness is k_{PTO}.

The model of the conventional type is illustrated in Fig. 1 (b). Let $z_k, (k = 1, 2)$ be the displacement of the kth body and z_s be the rotational displacement of the generator. Then we have

$$z_s = z_1 - z_2 \tag{1}$$

Hence the equation of motion of the floating buoy would be

$$m_1\ddot{z}_1 + m_s(\ddot{z}_1 - \ddot{z}_2) + (c_s + C_{\text{PTO}})(\dot{z}_1 - \dot{z}_2) + k_{\text{PTO}}(z_1 - z_2) = F_{d,1} + f_{w,1} \tag{2}$$

where m_1 is the mass of the floating buoy, m_s is the inertance caused by the generator itself, c_s is the unwanted inherent mechanical damping coefficient caused in the PTO system, C_{PTO} is the damping coefficient of the generator. Also, $f_{w,1}$ and $F_{d,1}$ are the hydrodynamic force and the drag force acting on the floating buoy, respectively.

While, the equation of motion of the submerged body is developed as

$$m_2\ddot{z}_2 - m_s(\ddot{z}_1 - \ddot{z}_2) - (c_s + C_{\text{PTO}})(\dot{z}_1 - \dot{z}_2) - k_{\text{PTO}}(z_1 - z_2) = F_{d,2} + f_{w,2} \tag{3}$$

where m_2 is the mass of the submerged body and $f_{w,2}$ and $F_{d,2}$ are the hydrodynamic force and the drag force on the submerged body, respectively, similarly to the floating buoy.

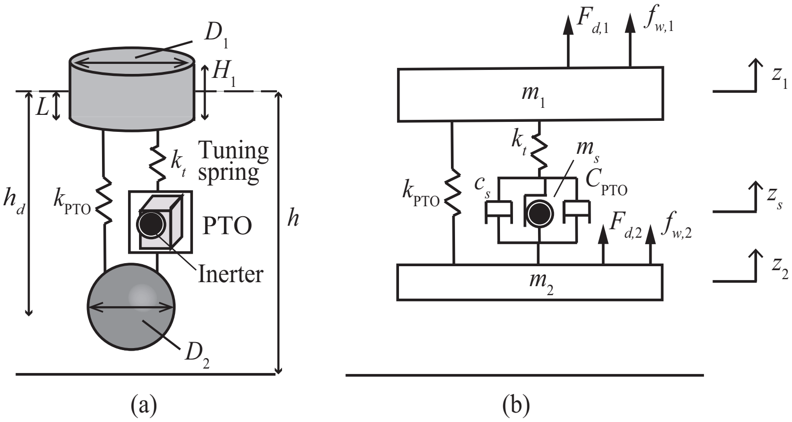

Figure 2: Two-body point absorber WEC with a tuned inerter: (a) Schematic illustration, (b) Model.

2.2. Two-body point absorber WEC with a tuned inerter

Next, the proposed two-body point absorber WEC with a tuned inerter shown in Fig. 2 (a) is considered. As can be seen, unlike the conventional two-body type, a tuning spring whose stiffness is k_t is added between the floating buoy and the PTO system. Also, an additional rotational mass such as a flywheel producing sufficiently large inertance m_s is mounted intentionally on the generator shaft.

The model of the present device is shown in Fig. 2 (b) and the equations of motion of the device are derived as follows. In contrast to the conventional type, Eq. (1) is not satisfied because the proposed system becomes a three-degree-of-freedom system due to the tuning spring. Then, for this model, the equations of motion of the floating buoy and the submerged body are given by

$$m_1\ddot{z}_1 + k_{\text{PTO}}(z_1 - z_2) + k_t(z_1 - z_2 - z_s) = F_{d,1} + f_{w,1} \tag{4}$$

$$m_2\ddot{z}_2 - k_{\text{PTO}}(z_1 - z_2) - k_t(z_1 - z_2 - z_s) = F_{d,2} + f_{w,2} \tag{5}$$

respectively. And considering the fact that the force of the tuning spring equals the force of the PTO system, the equation of motion of the inerter is derived as

$$m_s\ddot{z}_s + (c_s + C_{\text{PTO}})\dot{z}_s = k_t(z_1 - z_2 - z_s) \tag{6}$$

2.3. Hydrodynamic force

The hydrodynamic force $f_{w,k}$ acting on the kth body is described based on the linear potential wave theory by

$$f_{w,k} = f_{a,k} + f_{b,k} + f_{c,k} \tag{7}$$

where $f_{a,k}$ is the excitation force, $f_{b,k}$ is the hydrodynamic forces due to buoyancy, and $f_{c,k}$ is the radiation force.

The relationship between the excitation force $f_{a,k}$ and the amplitude of the incident wave $a(t)$ is given in the frequency domain using a transfer function $F_{a,k}(\omega)$ as

$$\hat{f}_{a,k}(\omega) = F_{a,k}(\omega)\hat{a}(\omega) \tag{8}$$

The hydrostatic force $f_{b,1}$ on the cylindrical floating buoy becomes a linear function of z_1 given as

$$f_{b,1} = -K_w z_1, \quad K_w = \rho g \pi \left(\frac{D_1}{2}\right)^2 \tag{9}$$

where g is gravitational acceleration and ρ is the sea water density. While the hydrostatic force of the submerged body is constant, thus $f_{b,2}$ can be set as

$$f_{b,2} = 0 \tag{10}$$

at the equilibrium position in the equation of motion.

Next, define $l = 1, 2, (l \neq k)$, then the radiation force $f_{c,k}$ on the kth body including the coupled force affected by the lth body is given by

$$\hat{f}_{c,k} = -(j\omega A_{kk}(\omega) + B_{kk}(\omega))\hat{\dot{z}}_k - (j\omega A_{kl}(\omega) + B_{kl}(\omega))\hat{\dot{z}}_l \tag{11}$$

where A_{kk} and B_{kk} are the added mass and the radiation damping of the kth body, and A_{kl} and B_{kl} represent the coupled added mass and the coupled radiation damping from the lth body to the kth body.

2.4. Drag force

The drag force $F_{d,k}$ acting on the kth body is modeled according to the nonlinear Morison equation given by [26]

$$F_{d,k} = -\frac{1}{2}\rho S_k C_{d,k}|\dot{z}_k|\dot{z}_k \tag{12}$$

where S_k is the characteristic area and $C_{d,k}$ is the dimensionless drag coefficient. As stated before, in this research, the shapes of the floating buoy and the submerged body are assumed to be a cylinder and a sphere, respectively, thus we have

$$S_1 = \frac{\pi D_1^2}{4}, \quad S_2 = \frac{\pi D_2^2}{4} \tag{13}$$

However, it would be cumbersome to deal with nonlinear equations in the frequency domain, Eq. (12) is linearized under the condition of irregular wave as [27, 26]

$$F_{d,k} = -\frac{1}{2}\rho S_k C_{d,k}\sqrt{\frac{8}{\pi}}\sigma_{\dot{z}_k}\dot{z}_k \tag{14}$$

where $\sigma_{\dot{z}_k}$ is the standard deviation of $\dot{z}_k$. While, in general, the drag force of the floating buoy is negligible compared to the hydrodynamic force, thus we assume that

$$F_{d,1} = 0 \tag{15}$$

From, Eq. (14), the linearized drag force on the submerged body is given with the viscous damping coefficient $c_{v,2}$ by

$$F_{d,2} = -c_{v,2}\dot{z}_2, \quad c_{v,2} = \frac{1}{2}\rho S_2 C_{d,2}\sqrt{\frac{8}{\pi}}\sigma_{\dot{z}_2} \tag{16}$$

Hereafter, in this article, $\sigma_{\dot{z}}$ is used to represent the standard deviation of $\dot{z}_2$ for simplicity.

2.5. Stochastic sea state model

In simple theoretical models of WECs, it is typical to assume the incident waves to be regular. For a more realistic model, irregular waves are used with time-domain analysis which requires much more computing time [4]. An alternative method with less computation for modeling true sea states is the stochastic modeling. We assume the wave amplitude $a(t)$ to be a stationary stochastic process with spectral density $S_a(\omega)$ and variance given by

$${\sigma_a}^2 = \frac{1}{2\pi}\int_{-\infty}^{\infty} S_a(\omega)d\omega \tag{17}$$

Characterizing $S_a(\omega)$ by the JONSWAP spectrum [28] with its mean wave period T_1, significant wave height H_s, and peak enhancement factor γ derives the following

$$S_a(\omega) = 310\pi \frac{H_s^2}{T_1^4 \omega^5} \exp\left[\frac{-944}{T_1^4 \omega^4}\right] \gamma^W \tag{18}$$

where

$$W = \exp\left[-\left(\frac{0.191\omega T_1 - 1}{\sqrt{2}\sigma}\right)^2\right] \tag{19}$$

and

$$\sigma = \begin{cases} 0.07 & : \omega T_1 \leq 5.24 \\ 0.09 & : \omega T_1 > 5.24 \end{cases} \tag{20}$$

The JONSWAP spectrum can also be represented by the peak period T_p using the well-known relationship

$$T_1 = 0.834 T_p \tag{21}$$

2.6. Power take-off system

In this study, the generator is assumed to be a three-phase permanent magnet synchronous machine (PMSM). However, the three phase voltage and current vectors can be transformed to "quadrature components". More details on this transformation can be found in [24, 29]. Then, assuming an ideal generator with linear behavior and minimal core loss results in linearity between the back-EMF e and the velocity coupled with the generator $\dot{z}_s$. Therefore, the equation relating to e and $\dot{z}_s$ is given as

$$e = K_e \dot{z}_s \tag{22}$$

where K_e is a constant associated with the back-EMF of the generator. By reciprocity, the electromagnetic force and generator current i has the following linear relationship

$$C_{\mathrm{PTO}} \dot{z}_s = -K_e i \tag{23}$$

In the case of single-directional converter used in [24], the input current to the generator i can be expressed as

$$i = -Ye \tag{24}$$

where Y is the admittance of the generator restricted in ideal conditions by [24]

$$Y \in [0, 1/R] \tag{25}$$

and R is the internal or coil resistance of the generator. Applying Eq. (24) to Eq. (23) with Eq. (22) yields

$$C_{\text{PTO}} = YK_e^2 \tag{26}$$

which expresses how the generator damping C_{PTO} is controlled by the admittance Y.

The total power generation is defined as the extracted power minus the electrical loss [10]. In this paper, we assume that the current-dependent loss is resistive, i.e., Ri^2, then we have the power generation as

$$P_g = -ei - Ri^2 \tag{27}$$

3. State-space representation

In this section, to assess the power generation by the current controllers under stochastic sea states, a state-space form of the proposed WEC augmented with the JONSWAP spectrum is developed. Also, the controllers for the current of the generator for power generation are reviewed briefly.

3.1. JONSWAP spectrum

First, a state-space model of the wave amplitude is derived. We find a finite-dimensional noise filter

$$F_w \sim \begin{bmatrix} \mathbf{A}_w & \mathbf{B}_w \\ \mathbf{C}_w & \mathbf{0} \end{bmatrix} \tag{28}$$

such that its power spectrum is close to the JONSWAP spectrum, i.e., $S_a(\omega) = |F_w(\omega)|^2$, for a unit intensity white noise input $w(t)$. Then we have

$$\begin{aligned} \dot{\mathbf{x}}_w(t) &= \mathbf{A}_w \mathbf{x}_w(t) + \mathbf{B} w(t) && (29) \\ a(t) &= \mathbf{C}_w \mathbf{x}_w(t) && (30) \end{aligned}$$

According to the simplified procedure advocated by Spanos [30], F_w can be approximated by a forth-order controllable canonical form of

$$\mathbf{A}_w = \begin{bmatrix} 0 & 1 & 0 & 0 \\ 0 & 0 & 1 & 0 \\ 0 & 0 & 0 & 1 \\ a_1 & a_2 & a_3 & a_4 \end{bmatrix}, \quad \mathbf{B}_w = \begin{bmatrix} 0 \\ 0 \\ 0 \\ 1 \end{bmatrix}, \quad \mathbf{C}_w = \begin{bmatrix} 0 & 0 & c_3 & 0 \end{bmatrix} \tag{31}$$

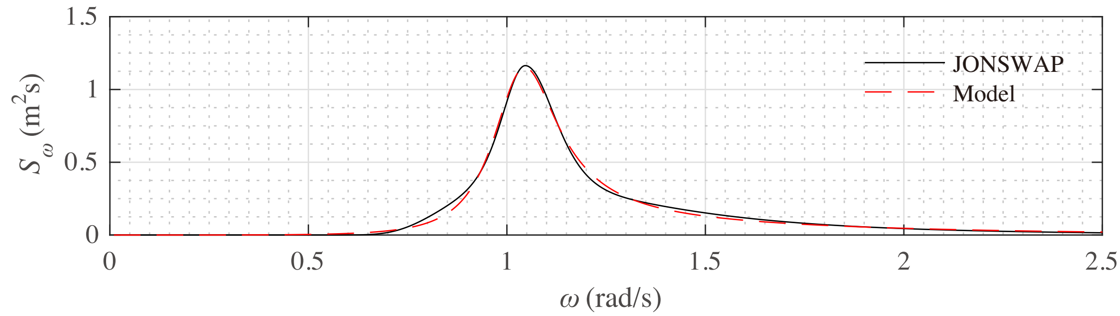

Figure 3: JONSWAP spectrum with T_p= 6 s, H_s= 1 m, γ = 3.3

where the filter parameters a_1, a_2, a_3, a_4, and c_3 are chosen to minimize the mean-square error $\int_{-\infty}^{\infty}(S_a(\omega) - |F_w(\omega)|^2)^2 d\omega$, while constraining a_1 through a_4 so that the system poles are in the open left half plane.

For example, Fig. 3 shows a JONSWAP spectrum for $T_p = 6$ s, $H_s = 1$ m, $\gamma = 3.3$ and its fourth-order finite-dimensional approximate system. We can confirm in the figure that the fourth-order F_w estimates the JONSWAP spectrum very well. It should be noted that $H_s = 1$ m, $\gamma = 3.3$ are fixed in the numerical simulation studies in this paper.

3.2. Two-body point absorber WEC with a tuned inerter

Next, state-space representation for the proposed device is developed here. As state-space representation for the conventional two-body WEC can be developed in a similar way, its derivation is omitted.

Substitute the equations for the hydrodynamic and drag forces into Eqs. (4) and (5), then taking Fourier transform gives

$$\begin{aligned} &\left\{-\omega^2(m_1 + A_{11}(\omega)) + j\omega(c_{v1} + B_{11}(\omega)) + (K_w + k_{\mathrm{PTO}} + k_t)\right\}\hat{z}_1 \\ &+ \left\{-\omega^2 A_{12}(\omega) + j\omega B_{12}(\omega) - (k_{\mathrm{PTO}} + k_t)\right\}\hat{z}_2 \\ &= F_{a,1}(\omega)\hat{a} + k_t\hat{z}_s \end{aligned} \tag{32}$$

and

$$\begin{aligned} &\left\{-\omega^2 A_{21}(\omega) + j\omega B_{21}(\omega) - (k_{\mathrm{PTO}} + k_t)\right\}\hat{z}_1 \\ &+ \left\{-\omega^2(m_2 + A_{22}(\omega)) + j\omega(c_{v2} + B_{22}(\omega)) + (k_{PTO} + k_t)\right\}\hat{z}_2 \\ &= F_{a,2}(\omega)\hat{a} - k_t\hat{z}_s \end{aligned} \tag{33}$$

respectively. Hence, Eqs. (32) and (33) can be combined and written in matrix form as

$$\begin{bmatrix} Z_{11} & Z_{12} \\ Z_{21} & Z_{22} \end{bmatrix} \begin{bmatrix} \hat{z}_1 \\ \hat{z}_2 \end{bmatrix} = \begin{bmatrix} F_{a,1} \\ F_{a,2} \end{bmatrix} \hat{a} + \begin{bmatrix} k_t \\ -k_t \end{bmatrix} \hat{z}_s \tag{34}$$

where

$$\begin{aligned} Z_{11}(\omega) &= -\omega^2(m_1 + A_{11}(\omega)) + j\omega(B_{11}(\omega)) + (K_w + k_{\mathrm{PTO}} + k_t) \\ Z_{12}(\omega) &= -\omega^2 A_{12}(\omega) + j\omega B_{12}(\omega) - (k_{\mathrm{PTO}} + k_t) \\ Z_{21}(\omega) &= -\omega^2 A_{21}(\omega) + j\omega B_{21}(\omega) - (k_{\mathrm{PTO}} + k_t) \\ Z_{22}(\omega) &= -\omega^2(m_2 + A_{22}(\omega)) + j\omega(c_{v,2} + B_{22}(\omega)) + (k_{\mathrm{PTO}} + k_t) \end{aligned} \tag{35}$$

Solving Eq. (34) for $\begin{bmatrix} \hat{z}_1 & \hat{z}_2 \end{bmatrix}^T$ yields the expressions of form

$$\hat{z}_1 = G_{a,1}(\omega)\hat{a} + G_{z,1}(\omega)\hat{z}_s \tag{36}$$

$$\hat{z}_2 = G_{a,2}(\omega)\hat{a} + G_{z,2}(\omega)\hat{z}_s \tag{37}$$

When $G_{a,1}$, $G_{z,1}$, $G_{a,2}$, and $G_{z,2}$ are approximated by finite-dimensional systems, we have representations as

$$G_{a,1} \sim \begin{bmatrix} \mathbf{A}_{a,1} & \mathbf{B}_{a,1} \\ \mathbf{C}_{a,1} & \mathbf{0} \end{bmatrix}, \quad G_{z,1} \sim \begin{bmatrix} \mathbf{A}_{z,1} & \mathbf{B}_{z,1} \\ \mathbf{C}_{z,1} & \mathbf{0} \end{bmatrix} \tag{38}$$

$$G_{a,2} \sim \begin{bmatrix} \mathbf{A}_{a,2} & \mathbf{B}_{a,2} \\ \mathbf{C}_{a,2} & \mathbf{0} \end{bmatrix}, \quad G_{z,2} \sim \begin{bmatrix} \mathbf{A}_{z,2} & \mathbf{B}_{z,2} \\ \mathbf{C}_{z,2} & \mathbf{0} \end{bmatrix} \tag{39}$$

It should be noted that the function $F_{a,k}$ in Eq. (8) is non-causal which will be problematic when approximating $G_{a,1}$ and $G_{a,2}$ by a finite-dimensional state-space. Therefore the technique of spatial delay proposed by Falnes [31] is used, defining $a(t)$ as the wave amplitude at a distance of d in front of the buoy.

Once Eqs. (38) and (39) are obtained by system identification techniques, the identified systems Eqs. (36) and (37) are represented in the time domain as

$$\dot{\mathbf{x}}_1(t) = \mathbf{A}_1\mathbf{x}_1(t) + \mathbf{G}_1 a(t) + \mathbf{E}_1 z_s(t) \tag{40}$$

$$z_1(t) = \mathbf{C}_1\mathbf{x}_1(t) \tag{41}$$

where $\mathbf{A}_1$, $\mathbf{G}_1$, $\mathbf{E}_1$, and $\mathbf{C}_1$ are expressed by $\mathbf{A}_{a,1}$, $\mathbf{B}_{a,1}$, $\mathbf{C}_{a,1}$, $\mathbf{A}_{z,1}$, $\mathbf{B}_{z,1}$, and $\mathbf{C}_{z,1}$. and

$$\begin{aligned} \dot{\mathbf{x}}_2(t) &= \mathbf{A}_2\mathbf{x}_2(t) + \mathbf{G}_2 a(t) + \mathbf{E}_2 z_s(t) &(42)\\ z_2(t) &= \mathbf{C}_2\mathbf{x}_2(t) &(43)\end{aligned}$$

where $\mathbf{A}_2$, $\mathbf{G}_2$, $\mathbf{E}_2$, and $\mathbf{C}_2$ are expressed by $\mathbf{A}_{a,2}$, $\mathbf{B}_{a,2}$, $\mathbf{C}_{a,2}$, $\mathbf{A}_{z,2}$, $\mathbf{B}_{z,2}$, and $\mathbf{C}_{z,2}$ as well.

Also, considering $z_1 - z_2$ as an input, we have a state-space representation about the tuned inerter part where the output is the velocity of the generator as

$$\begin{aligned} \dot{\mathbf{x}}_s(t) &= \mathbf{A}_s\mathbf{x}_s(t) + \mathbf{B}_s i(t) + \mathbf{E}_s(z_1(t) - z_2(t)) &(44)\\ \dot{z}_s(t) &= \mathbf{C}_s\mathbf{x}_s(t) &(45)\end{aligned}$$

where the state vector is defined as $\mathbf{x}_s = \begin{bmatrix} z_s & \dot{z}_s \end{bmatrix}^T$ and

$$\mathbf{A}_s = \begin{bmatrix} 0 & 1 \\ -\frac{k_t}{m_s} & -\frac{c_s}{m_s} \end{bmatrix}, \quad \mathbf{B}_s = \begin{bmatrix} 0 \\ \frac{c_e}{m_s} \end{bmatrix}, \quad \mathbf{E}_s = \begin{bmatrix} 0 \\ \frac{k_t}{m_s} \end{bmatrix}, \quad \mathbf{C}_s = \begin{bmatrix} 0 & 1 \end{bmatrix} \tag{46}$$

Define the state vector as $\mathbf{x}_h = \begin{bmatrix} \mathbf{x}_1^T & \mathbf{x}_2^T & \mathbf{x}_s^T \end{bmatrix}^T$. Then we have a state-space representation in which the inputs are the current i and the wave height a and the output is the voltage e from Eq. (22) and Eqs. (40) through (46) as follows:

$$\begin{aligned} \dot{\mathbf{x}}_h(t) &= \mathbf{A}_h\mathbf{x}_h(t) + \mathbf{B}_h i(t) + \mathbf{G}_h a(t) &(47)\\ e(t) &= \mathbf{C}_h\mathbf{x}_h(t) &(48)\end{aligned}$$

where $\mathbf{A}_h$, $\mathbf{B}_h$, $\mathbf{G}_h$, and $\mathbf{C}_h$ can be composed of $\mathbf{A}_1$, $\mathbf{A}_2$, $\mathbf{B}_1$, $\mathbf{B}_2$, $\mathbf{G}_1$, $\mathbf{G}_2$, $\mathbf{C}_1$, $\mathbf{C}_2$, $\mathbf{A}_s$, $\mathbf{B}_s$, $\mathbf{E}_s$, and $\mathbf{C}_s$.

3.3. Augmented system

Finally, combining Eqs. (47) and (48) with the stochastic sea state model given by Eqs. (29) and (30) gives the augmented system where the external disturbance input is white noise $w(t)$ expressed as

$$\begin{aligned} \dot{\mathbf{x}}(t) &= \mathbf{A}\mathbf{x}(t) + \mathbf{B}i(t) + \mathbf{G}w(t) &(49)\\ e(t) &= \mathbf{C}\mathbf{x}(t) &(50)\end{aligned}$$

where

$$\mathbf{x} = \begin{bmatrix} \mathbf{x}_h \\ \mathbf{x}_w \end{bmatrix}, \ \mathbf{A} = \begin{bmatrix} \mathbf{A}_h & \mathbf{G}_h\mathbf{C}_w \\ \mathbf{0} & \mathbf{A}_w \end{bmatrix}, \ \mathbf{B} = \begin{bmatrix} \mathbf{B}_h \\ \mathbf{0} \end{bmatrix}, \ \mathbf{G} = \begin{bmatrix} \mathbf{0} \\ \mathbf{B}_w \end{bmatrix}, \ \mathbf{C} = \begin{bmatrix} \mathbf{C}_h & \mathbf{0} \end{bmatrix} \tag{51}$$

3.4. Controller

To improve the power generation performance and to examine the effectiveness of the current control on the proposed device, the current of the generator i is controlled by the two control laws introduced in [24] which are reviewed briefly here. Before we go any further, it should be noted that the average of the generated power defined as Eq. (27) can be written as

$$\bar{P}_g = -\varepsilon \left\{ \begin{bmatrix} \mathbf{x} \\ i \end{bmatrix}^T \begin{bmatrix} \mathbf{0} & \frac{1}{2}\mathbf{C}^T \\ \frac{1}{2}\mathbf{C} & R \end{bmatrix} \begin{bmatrix} \mathbf{x} \\ i \end{bmatrix} \right\} \tag{52}$$

using Eq. (50).

3.4.1. Static admittance control

For the SA control, a constant feedback gain Y_c restricted by Eq. (25) is adopted so that the value defined by Eq. (52) is maximized. The method to search for such a value is reviewed here.

From Eqs. (24) and (50), the input current to the generator is expressed as a function of the state variable $\mathbf{x}$, i.e.,

$$i(t) = -Y_c\mathbf{C}\mathbf{x}(t) \tag{53}$$

Substituting Eq. (53) into Eq. (49) yields the closed-loop dynamics having the form

$$\dot{\mathbf{x}}(t) = (\mathbf{A} - Y_c\mathbf{B}\mathbf{C})\mathbf{x}(t) + \mathbf{G}w(t) \tag{54}$$

Let the average power by the SA control be $\bar{P}_g^{\mathrm{SA}}$. Then for any time-invariant Y_c satisfying Eq. (25), it is a standard result that the power generation objective can be written as [32]

$$\bar{P}_g^{\mathrm{SA}} = -\,\mathrm{tr}[\mathbf{G}^T\mathbf{S}\mathbf{G}] \tag{55}$$

where $\mathbf{S} = \mathbf{S}^T < 0$ is the solution to the Lyapunov equation

$$(\mathbf{A} - Y_c\mathbf{B}\mathbf{C})^T\mathbf{S} + \mathbf{S}(\mathbf{A} - Y_c\mathbf{B}\mathbf{C}) + \mathbf{C}^T(-Y_c + Y_c^2R)\mathbf{C} = \mathbf{0} \tag{56}$$

Y_c must be less than or equal to $1/R$, so the last term on the left-hand side of Eq. (56) is negative-semidefinite for all Y_c. Thus, since $\mathbf{A} - Y_c\mathbf{B}\mathbf{C}$ is asymptotically stable, the definiteness of $\mathbf{S}$ is assured by Lyapunov's second theorem [33]. Then the optimal value for Y_c is chosen so that Eq. (55) is maximized.

3.4.2. Performance guaranteed control

For comparison, the efficacy of time-varying gain Y based on the PG control algorithm proposed in the literature is examined. This algorithm is operated with a single-directional converter and the admittance Y becomes a function of time varying within the range of Eq. (25) so that the generated average power $\bar{P}_g^{\mathrm{PG}}$ must be larger than $\bar{P}_g^{\mathrm{SA}}$, i.e.,

$$\bar{P}_g^{\mathrm{PG}} \geq \bar{P}_g^{\mathrm{SA}} \tag{57}$$

In this algorithm, the admittance is controlled by

$$Y(t) = \underset{[0,1/R]}{\mathrm{sat}} \left\{ \frac{\mathbf{Kx}}{e} \right\} \tag{58}$$

where

$$\mathbf{K} = -\frac{1}{R}\left(\mathbf{B}^T\mathbf{S} + \frac{1}{2}\mathbf{C}\right) \tag{59}$$

Note that Y_c is the constant value for the SA control. In this case, the current i is expressed by

$$i(t) = \begin{cases} i_u(t) & : i_u e + i_u^2 R \leq 0 \\ 0 & : i_u e + i_u^2 R > 0 \ \text{ and } \ i_u e > 0 \\ -e(t)/R & : \text{otherwise} \end{cases} \tag{60}$$

where

$$i_u = \mathbf{Kx} \tag{61}$$

And the generated average energy would be

$$\bar{P}_g^{\mathrm{PG}} = \bar{P}_g^{\mathrm{SA}} + R\,\mathcal{E}\left\{(i_u + Y_c e)^2 - (i_u - i)^2\right\} \tag{62}$$

which guarantees the inequality given by Eq. (57).

4. Numerical simulation

To verify the efficacy of the proposed two-body point absorber WEC, numerical simulation studies are carried out in this section. First, the parameter values of the model used here are developed, then the power generation performance is assessed.

Table 1: Parameter values for numerical simulation

Parameter	Value	Parameter	Value
m_1	58,075 kg	m_2	34,515 kg
D_1	6.0 m	D_2	4.0 m
H_1	2.5 m	L	2.0 m
h	400 m	h_d	20 m
k_t	10,000 N/m	k_{PTO}	100,000 N/m
c_s	50 Ns/m	$C_{d,2}$	0.1
R	25 Ω	ρ	1,027 kg/m^3

4.1. Model development

The parameter values for the two-body point absorber used here is determined based on the study conducted in [20], which are summarized in Table 1.

The added mass and the radiation damping of the floating buoy and the submerged body calculated using WAMIT software [25] are shown in Figs. 4 and 5, respectively. The magnitude and the phase of the transfer functions given by Eq. (8) are shown in the figures as well. Moreover, the coupled added mass and radiation damping acting on the floating buoy from the submerged body, i.e., A_{12} and B_{12} and vice versa, i.e., A_{21} and B_{21} are shown in Fig. 6.

Then, from Eqs. (34) and (35), the frequency response data for $G_{a,1}$, $G_{z,1}$, $G_{a,2}$, and $G_{z,2}$ in Eqs. (36) and (37) are calculated as depicted in Figs. 7 and 8 by solid lines. Then, to express these in state-space form as expressed by Eqs. (38) and (39), $G_{a,1}$ and $G_{a,2}$ are approximated with 5 zeros and 6 poles, and $G_{z,1}$ with 2 zeros and 4 poles, and $G_{z,2}$ with 4 zeros and 5 poles. These numbers are chosen by trial and error so that the finite-dimensional models shown by dashed lines approximate the frequency response data very well. Note that the wave amplitude $a(t)$ is taken to be the wave amplitude $d = 10$ m ahead of the buoy in the propagation direction.

4.2. Inerter design

Next, the inertance m_s for the proposed WEC needs to be designed. In this study, this value is chosen so that the average power generation for the JONSWAP spectrum with $T_p = 6$ s is maximized when the SA controller is applied. While the damping coefficient of the drag force on the submerged

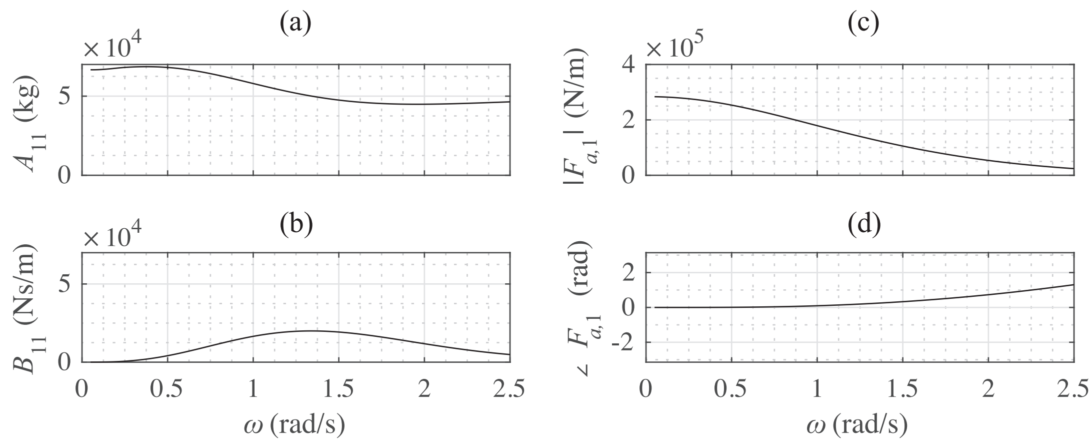

Figure 4: Hydrodynamic parameters for the heave mode of the floating buoy : (a) Added mass A_{11}, (b) Radiation damping B_{11}, (c) Magnitude of $F_{a,1}(\omega)$, (d) Phase of $F_{a,1}(\omega)$.

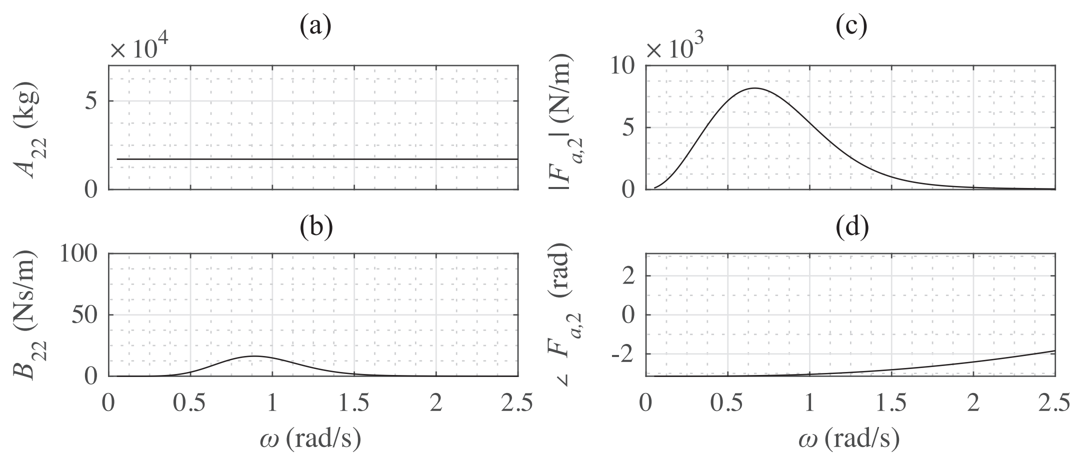

Figure 5: Hydrodynamic parameters for the heave mode of the submerged body : (a) Added mass A_{22}, (b) Radiation damping B_{22}, (c) Magnitude of $F_{a,2}(\omega)$, (d) Phase of $F_{a,2}(\omega)$.

body given by (16) depends on the standard deviation of the velocity $\dot{z}_2$. Thus, the value m_s is designed according to the flowchart as shown in Fig. 9 (a) here, in which $\sigma_{\dot{z}}^-$ and $\sigma_{\dot{z}}$ are standard deviations at the previous and current iterations, respectively. This flowchart is made based on the method to determine $\sigma_{\dot{z}}$ introduced in [26]. For this iteration process, the initial value for $\sigma_{\dot{z}}$ is set to $\sigma_{\dot{z}0} = 0.1$ m/s and the range for m_s is set between $m_{s0} = 5,000$ kg and $m_{se} = 10,000$ kg and the best value is sought with respect to each

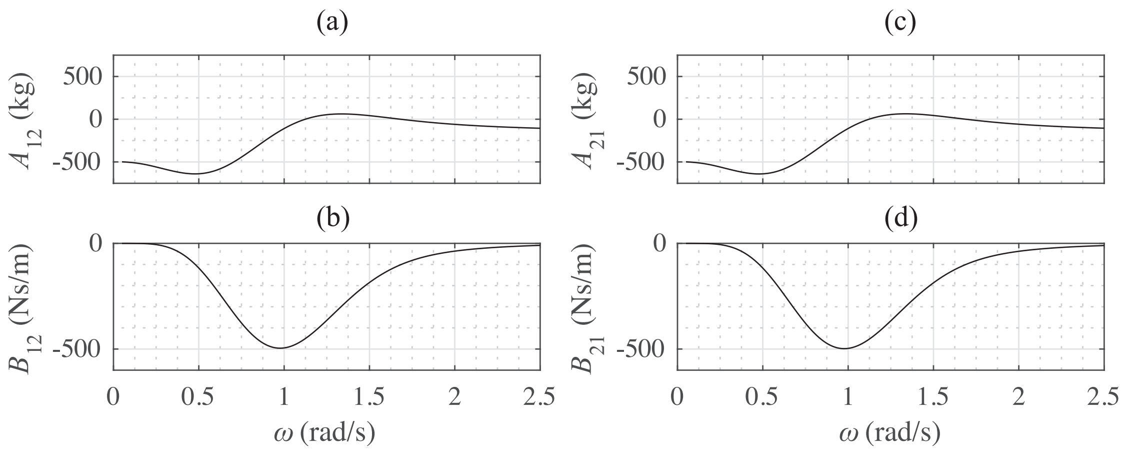

Figure 6: Coupled hydrodynamic parameters for the heave mode of the two bodies : (a) Added mass, A_{12} (b) Radiation damping B_{12}, (c) Added mass Added mass, A_{21}, (d) Radiation damping B_{21}.

100 kg iteratively.

During the iteration, the standard deviation of $\dot{z}_2$ is calculated simply from

$$\sigma_{\dot{z}}^2 = \mathbf{G}^T \mathbf{S}_{\dot{z}} \mathbf{G} \tag{63}$$

where $\mathbf{S}_{\dot{z}} = \mathbf{S}_{\dot{z}}^T > 0$ is the solution to the Lyapunov equation

$$(\mathbf{A} - Y_c \mathbf{BC})^T \mathbf{S}_{\dot{z}} + \mathbf{S}_{\dot{z}} (\mathbf{A} - Y_c \mathbf{BC}) + \mathbf{C}_{\dot{z}}^T \mathbf{C}_{\dot{z}} = \mathbf{0} \tag{64}$$

and

$$\dot{z}_2 = \mathbf{C}_{\dot{z}} \mathbf{x} \tag{65}$$

Then, if the difference between the obtained $\sigma_{\dot{z}}$ and the previous value $\sigma_{\dot{z}}^-$ is larger than 0.001, the damping coefficient for the linearized drag force is recalculated using the newly obtained $\sigma_{\dot{z}}$ from Eq. (16). This procedure continues until the value of the standard deviation converges enough. And the average power for the SA control is calculated using the converged $\sigma_{\dot{z}}$ from Eq. (55)

The average power obtained in the process of the flowchart is plotted in Fig. 10. As can be seen, the generation performance peaks at $m_s = 6,900$ kg, which is used for the numerical simulation studies.

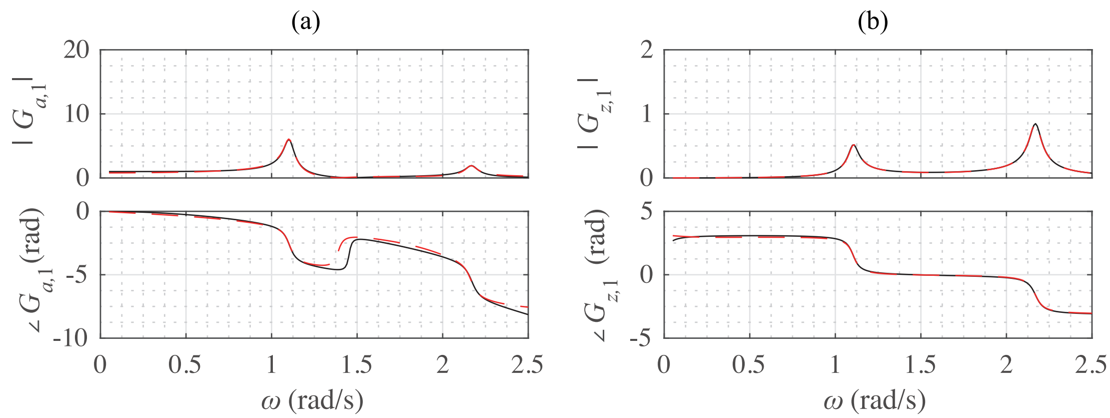

Figure 7: Frequency domain data (solid) and finite-dimensional approximation (dashed) : (a) $G_{a,1}(\omega)$, (b) $G_{z,1}(\omega)$.

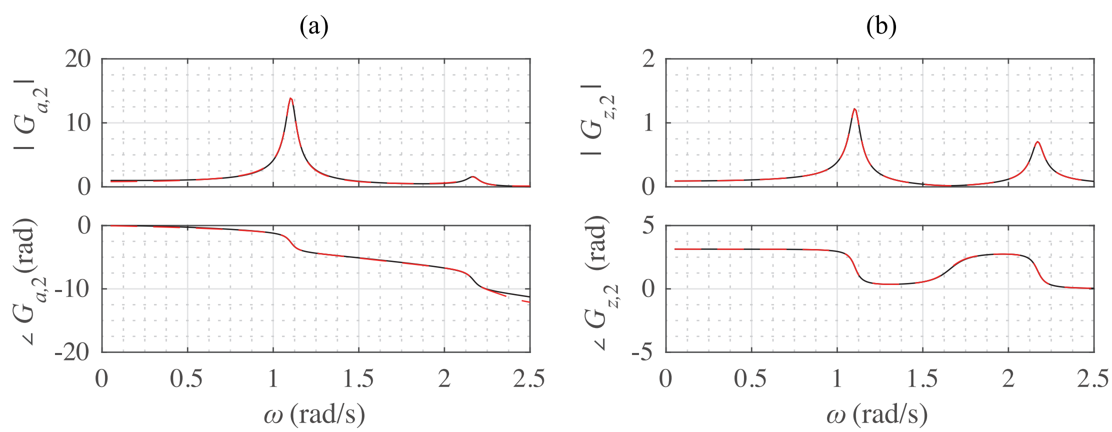

Figure 8: Frequency domain data (solid) and finite-dimensional approximation (dashed) : (a) $G_{a,2}(\omega)$, (b) $G_{z,2}(\omega)$.

4.3. Drag force model

The damping coefficient $c_{v,2}$ for the linearized drag force acting on the submerged body as expressed by Eq. (16) still needs to be obtained for each peak wave period T_p. The inertance value is set to $m_s = 6,900$ kg as determined before. Then we seek for the damping coefficient value for each T_p of the JONSWAP spectrum based on the flowchart shown in Fig. 9 (b). This is referred to the flowchart in [26] as well as Fig. 9 (a). For the process, $\sigma_{\dot{z}}$ is first set to $\sigma_{\dot{z}0} = 0.1$ m/s as well as before and $c_{v,2}$ is investigated in the range of the peak wave period T_p from 2 s and 12 s, i.e., we set $T_{p0} = 2$

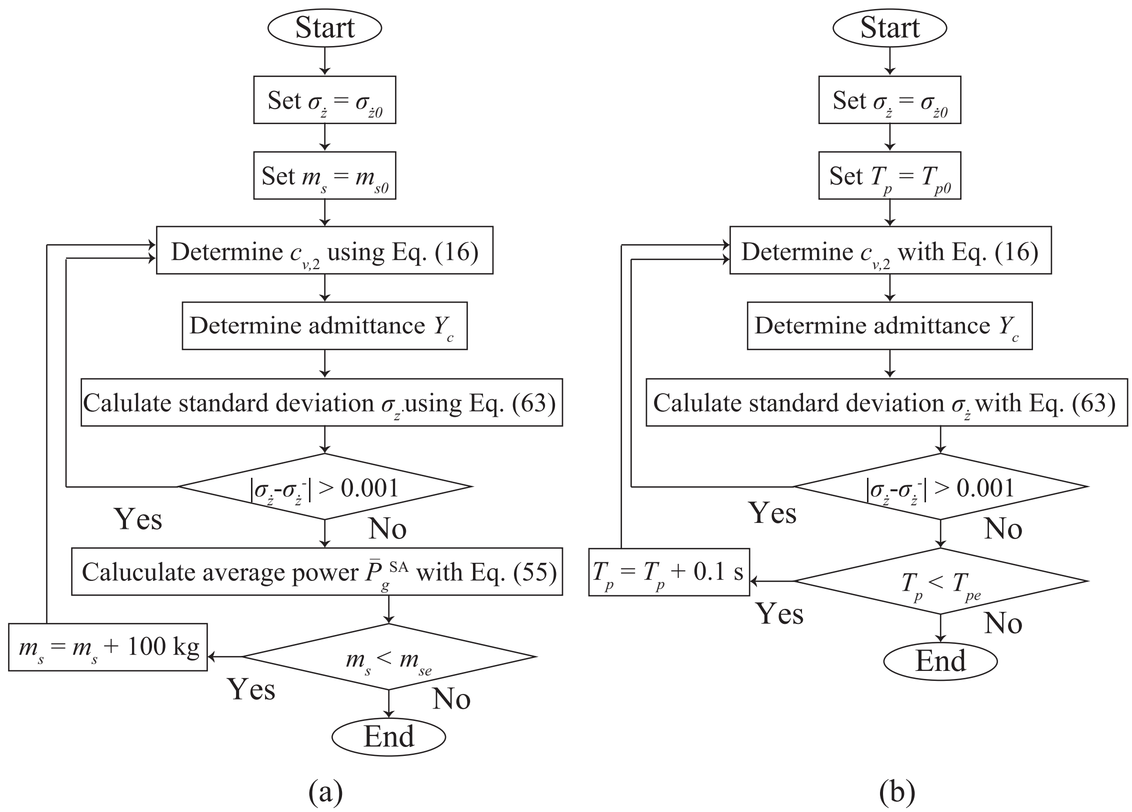

Figure 9: Flowchart: (a) Inerter design, (b) Drag force model.

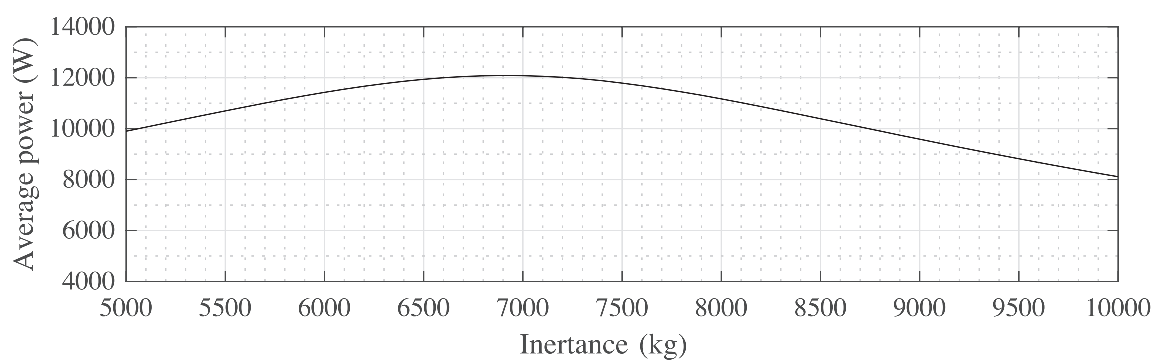

Figure 10: Average power vs inerter.

341 s and $T_{pe} = 12$ s.

342 The result for the case of the two-body point absorber with a tuned inerter

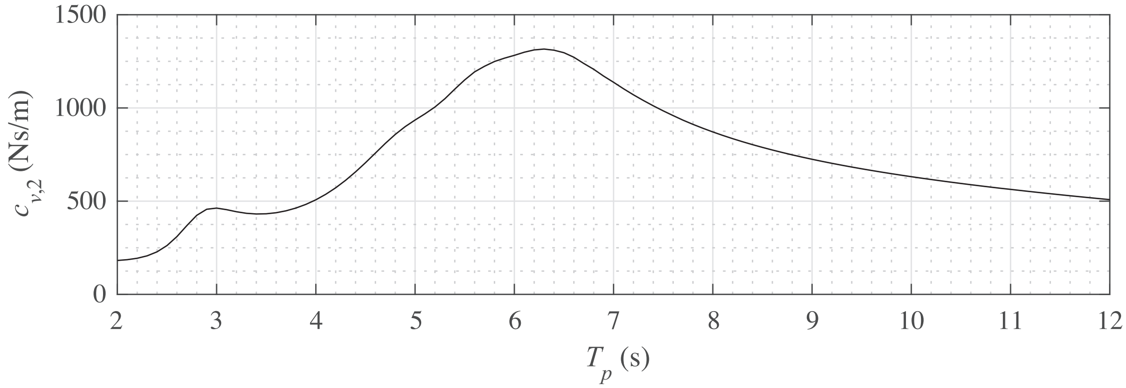

Figure 11: Damping coefficient $c_{v,2}$ for the drag force on the submerged body.

of $m_s = 6,900$ kg is shown in Fig. 11. We can find that $c_{v,2}$ is much larger than the radiation damping on the submerged body denoted by B_{22} and confirm that the drag force on the submerged body should not be ignored.

4.4. Results

Finally, the average power generations for the JONSWP spectrum with the peak wave period from 2 s to 12 s are calculated from the parameter values determined above.The results obtained from the SA and the PG controllers are compared in Fig. 12 (a), in which the proposed point absorber WEC with a tuned inerter and the conventional WEC cases are denoted by 2BwTI and 2B, respectively. The average power for the SA control cases can be given by the closed form expressed by Eq. (55), however, for consistency with the PG control cases, the average values shown in Fig. 12 (a) are calculated from Eq. (27) using the numerical simulation results for 100,000 s. The admittances for the SA controller are compared in Fig. 12 (b) which shows the difference of the optimized admittance between the proposed and the conventional WECs. For the assessment of the conventional WEC, the same parameters as the proposed WEC are employed except that $m_s = 50$ kg. As you can see in Fig. 12 (a), the proposed WEC shows the better power generation performance than the conventional WEC in the wide range of the peak wave period T_p even though the effectiveness deteriorates in a certain range of the lower period. Especially, the superiority of the proposed WEC is notable around $T_p = 6$ s to which the inerter of the proposed WEC is designed to be tuned. Also, the PG controller works well to improve the power generation especially for the proposed WEC.

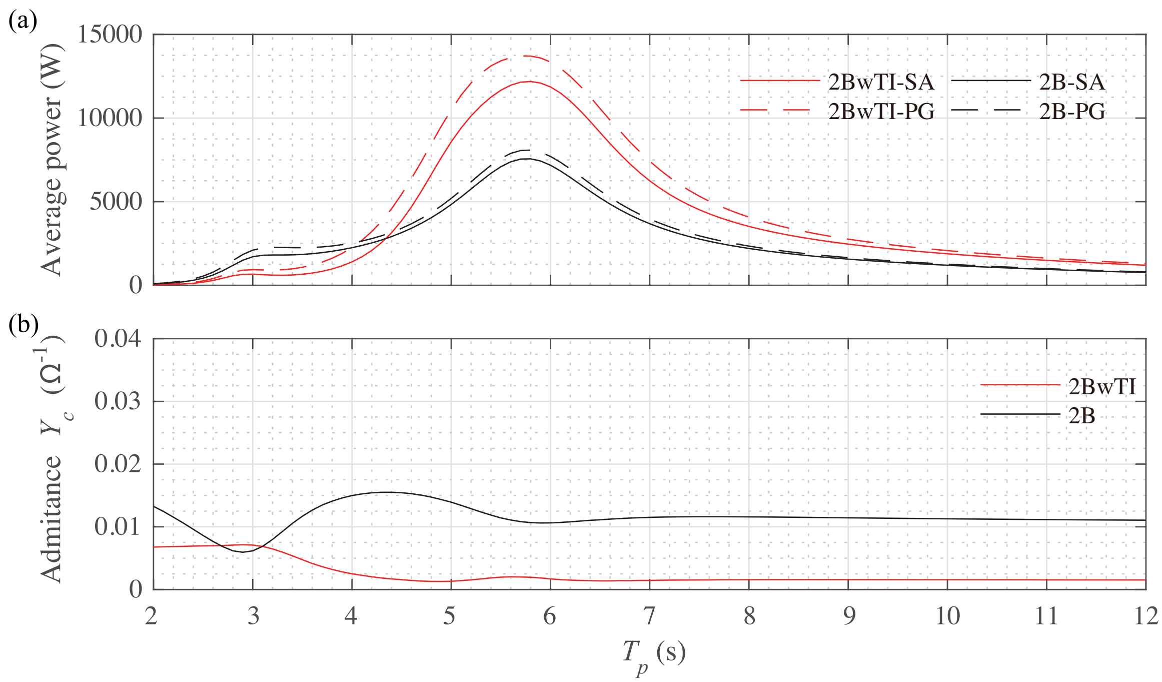

Figure 12: Results. (a) Power generation, (b) Admittance.

5. Conclusions

This article introduced the two-body point absorber WEC with a tuned inerter and developed the detailed analytical model including the coupled force between the two bodies. Then its effectiveness was verified by comparing the conventional two-body point absorber WEC through the numerical simulation studies. The results showed that the tuned inerter mechanism not only increased the power generation performance but also broadened the effective range of the wave period. Moreover, this research showed that the performance of the proposed WEC was improved further by controlling the current of the generator.

However, the optimum design including the shapes of the floating buoy and the submerged body should be examined more thoroughly, for example, by a CFD (computational fluid dynamics) technique. And various control algorithms such as reactive controllers should be applied to the generator current of the proposed WEC or more effecitve controllers need to be developed. In addition, experimental verification is still required to show the reliability of the proposed WEC.

Acknowledgments

The authors gratefully acknowledge support for this research through JSPS KAKENHI Grant number 18K189808 and TEPCO (Tokyo Electric Power Company) Memorial Foundation.

References

[1] Y. Masuda, An experience of wave power generator through tests and improvement, in: D. V. Evans, A. F. O. de Falcão (Eds.), Hydrodynamics of Ocean Wave-Energy Utilization, Springer Berlin Heidelberg, Berlin, Heidelberg, 1986, pp. 445–452.

[2] M. McCormick, Ocean Wave Energy Conversion, Dover Civil and Mechanical Engineering Series, Dover Publications, 2007.

[3] J. Falnes, A review of wave-energy extraction, Marine Structures 20 (4) (2007) 185 – 201. doi:https://doi.org/10.1016/j.marstruc.2007.09.001.

[4] A. F. de O. Falcão, Wave energy utilization: A review of the technologies, Renewable and Sustainable Energy Reviews 14 (3) (2010) 899 – 918. doi:https://doi.org/10.1016/j.rser.2009.11.003.

[5] E. Rusu, F. Onea, A review of the technologies for wave energy extraction, Clean Energy 2 (1) (2018) 10–19. doi:10.1093/ce/zky003.

[6] A. F. Falcão, J. C. Henriques, Oscillating-water-column wave energy converters and air turbines: A review, Renewable Energy 85 (2016) 1391 – 1424. doi:https://doi.org/10.1016/j.renene.2015.07.086.

[7] D. V. EVANS, The Oscillating Water Column Wave-energy Device, IMA Journal of Applied Mathematics 22 (4) (1978) 423–433. doi:10.1093/imamat/22.4.423.

[8] K. Budar, J. Falnes, A resonant point absorber of ocean-wave power, Nature 256 (5517) (1975) 478.

[9] J. Falnes, Ocean Waves and Oscillating Systems: Linear Interactions Including Wave-Energy Extraction, Cambridge University Press, 2002. doi:10.1017/CBO9780511754630.

[10] J. Scruggs, S. Lattanzio, A. Taflanidis, I. Cassidy, Optimal causal control of a wave energy converter in a random sea, Applied Ocean Research 42 (2013) 1 – 15. doi:https://doi.org/10.1016/j.apor.2013.03.004.

[11] P. Contestabile, G. Crispino, E. Di Lauro, V. Ferrante, C. Gisonni, D. Vicinanza, Overtopping breakwater for wave energy conversion: Review of state of art, recent advancements and what lies ahead, Renewable Energy 147 (2020) 705 – 718. doi:https://doi.org/10.1016/j.renene.2019.08.115.

[12] L. Margheritini, D. Vicinanza, P. Frigaard, Ssg wave energy converter: Design, reliability and hydraulic performance of an innovative overtopping device, Renewable Energy 34 (5) (2009) 1371 – 1380. doi:https://doi.org/10.1016/j.renene.2008.09.009.

[13] J. P. Kofoed, P. Frigaard, E. Friis-Madsen, H. C. Sørensen, Prototype testing of the wave energy converter wave dragon, Renewable Energy 31 (2) (2006) 181 – 189, marine Energy. doi:https://doi.org/10.1016/j.renene.2005.09.005.

[14] R. Haraguchi, T. Asai, Enhanced power absorption of a point absorber wave energy converter using a tuned inertial mass, Energy 202 (2020) 117740. doi:https://doi.org/10.1016/j.energy.2020.117740.

[15] K. Sugiura, R. Sawada, Y. Nemoto, R. Haraguchi, T. Asai, Wave flume testing of an oscillating-body wave energy converter with a tuned inerter, Applied Ocean Research 98 (2020) 102127. doi:https://doi.org/10.1016/j.apor.2020.102127.

[16] K. Ikago, K. Saito, N. Inoue, Seismic control of single-degree-of-freedom structure using tuned viscous mass damper, Earthquake Engineering & Structural Dynamics 41 (3) 453–474. doi:10.1002/eqe.1138.

[17] M. C. Smith, Synthesis of mechanical networks: The inerter, Proceedings of the IEEE Conference on Decision and Control 2 (10) (2002) 1657–1662. doi:10.1109/cdc.2002.1184758.

[18] T. Asai, Y. Araki, K. Ikago, Energy harvesting potential of tuned inertial mass electromagnetic transducers, Mechanical Systems and Signal Processing 84 (2017) 659 – 672. doi:https://doi.org/10.1016/j.ymssp.2016.07.048.

[19] K. Sugiura, Y. Watanabe, T. Asai, Y. Araki, K. Ikago, Experimental characterization and performance improvement evaluation of an electromagnetic transducer utilizing a tuned inerter, Journal of Vibration and Control 26 (1-2) (2020) 56–72. doi:10.1177/1077546319876396.

[20] E. A. Shami, X. Wang, R. Zhang, L. Zuo, A parameter study and optimization of two body wave energy converters, Renewable Energy 131 (2019) 1 – 13. doi:https://doi.org/10.1016/j.renene.2018.06.117.

[21] D. Martin, X. Li, C.-A. Chen, K. Thiagarajan, K. Ngo, R. Parker, L. Zuo, Numerical analysis and wave tank validation on the optimal design of a two-body wave energy converter, Renewable Energy 145 (2020) 632 – 641. doi:https://doi.org/10.1016/j.renene.2019.05.109.

[22] E. Anderlini, D. Forehand, E. Bannon, Q. Xiao, M. Abusara, Reactive control of a two-body point absorber using reinforcement learning, Ocean Engineering 148 (2018) 650 – 658. doi:https://doi.org/10.1016/j.oceaneng.2017.08.017.

[23] X. Li, D. Martin, C. Liang, C. Chen, R. G. Parker, L. Zuo, Characterization and verification of a two-body wave energy converter with a novel power take-off, Renewable Energy-doi:https://doi.org/10.1016/j.renene.2020.08.113.

[24] I. L. Cassidy, J. T. Scruggs, Nonlinear stochastic controllers for power-flow-constrained vibratory energy harvesters, Journal of Sound and Vibration 332 (13) (2013) 3134 – 3147. doi:https://doi.org/10.1016/j.jsv.2013.01.023.

[25] WAMIT, Inc., WAMIT, `http://www.wamit.com/index.htm`, MA, USA (2020).

[26] C. O. Housseine, C. Monroy, G. de Hauteclocque, Stochastic Linearization of the Morison Equation Applied to an Offshore Wind Turbine, in: Volume 9: Ocean Renewable Energy, American Society of Mechanical Engineers, 2015. doi:10.1115/OMAE2015-41301.

[27] N. H. Thinh, N. D. Anh, D. A. Cuong, An equivalent linearization for the drag force in the Morison's equation using Hermite polynomial error sample function, Vietnam Journal of Mechanics 20 (2) (1998) 55–64. doi:10.15625/0866-7136/10021.

[28] O. Faltinsen, Sea Loads on Ships and Offshore Structures, Cambridge Ocean Technology Series, Cambridge University Press, 1993.

[29] R. R. Krishnan, Electric motor drives : modeling, analysis, and control, Upper Saddle River, N.J. : Prentice Hall, 2001, includes bibliographical references and index.

[30] P.-T. Spanos, Filter approaches to wave kinematics approximation, Applied Ocean Research 8 (1) (1986) 2 – 7. doi:https://doi.org/10.1016/S0141-1187(86)80025-6.

[31] J. Falnes, On non-causal impulse response functions related to propagating water waves, Applied Ocean Research 17 (6) (1995) 379–389. doi:10.1016/S0141-1187(96)00007-7.

[32] P. Dorato, C. Abdallah, V. Cerone, Linear Quadratic Control: An Introduction, Krieger Publishing Company, 1995.

[33] R. Stengel, Optimal Control and Estimation, Dover books on advanced mathematics, Dover Publications, 1986.